Investigating off-road vehicle lateral stability with integrated chassis control

Simon J. Scholtz[a] and Herman A. Hamersma[b*]

[a,b]*Department of Mechanical and Aeronautical Engineering, University of Pretoria, Pretoria, South Africa*

[*]Herman A. Hamersma <herman.hamersma@up.ac.za>

This study investigates the improvement of off-road vehicle lateral stability by integrated control of active rear steering (ARS) and rear differential braking (RDB) and how the performance of such systems compares on smooth and rough roads. The ARS and RDB controllers comprise a sliding mode controller (SMC) for which critical design choices are the SMC reference model, SMC gain, and integration rule. Findings include that the kinematic model reference error is preferred over the phase plane location error on both terrains, the SMC gain is terrain dependent, and the rear axle slip angle is the preferred integration rule over the stability index (SI) on both terrains. The study also found that RDB, and to a lesser degree ARS, tend to improve on the baseline vehicle path-following ability for a double lane change (DLC) manoeuvre on both terrains, but RDB has a larger loss of speed compared to ARS. The Rear axle slip angle was found to be a terrain-dependent tuneable integration rule to combine ARS and RDB, and this resulted in a control system that has the good path-following ability of RDB but the low loss of speed associated with ARS after tuning.

Keywords: stability control; integrated chassis control (ICC); active rear steering; differential braking; sliding mode stability control; off-road vehicle dynamics

Introduction

Vehicle loss of control (LOC) is a major contributor to road traffic accidents that, combined with other causes, lead to 1.35 million road accident deaths globally [1]. An established solution to LOC is the electronic stability control (ESC) developed by

Bosch, first implemented on a commercial vehicle in 1995 [2]. ESC uses differential braking to brake individual wheels to generate a restoring yaw moment that counters the LOC motion. Several studies have confirmed the positive impact of ESC on reducing road accidents and fatalities [3,4].

A comparable solution to ESC is active steering (AS), which is a tyre steering method for controlling vehicle yaw or sideslip angle, based on either improving driver comfort or as a stability control strategy. AS can be used as an alternative to, or in combination with, brake-based stability control. ESC and AS are examples of chassis control systems that are collectively referred to as advanced driver assistance systems (ADAS), all of which improve vehicle safety directly or indirectly.

While studies indicate that stand-alone chassis control systems are effective at accident prevention [3], the forefront of ADAS and chassis control research is on the integration of individual sub-systems called integrated chassis control (ICC). ICC increases the utilization of the available tyre-road friction leading to a greater range of vehicle stability compared to stand-alone systems; this improves overall vehicle safety [5].

A plethora of on-road ICCs exist in the literature for improved vehicle lateral stability, while off-road specific ADAS and ICC systems research is sparse. ICCs are largely developed for on-road vehicles driving in on-road conditions while off-road vehicles, posing a unique risk due to factors such as a higher centre of gravity (CG), soft suspension and rough road excitations, have not received the same attention [6,7].

This study considers the integration of active rear steering (ARS) and rear differential braking (RDB). Differential braking is an existing control strategy for ESC

equipped commercial vehicles that imposes longitudinal force on the to generate a restoring yaw moment while simultaneously reducing vehicle speed. ARS imposes lateral forces on the vehicle and has a lower utilization of tyre-road friction to generate the same yaw moment compared to differential braking [8]. This is due to the increased moment arm associated with steering (dependent on wheelbase) compared to braking (dependent on trackwidth). Their distinct advantages make ARS and RDB a popular on-road vehicle integration format [5].

1.1 RDB and ARS systems in literature

Canale & Fagiano [9] compared the performance of stand-alone RDB and ARS systems for stability control. They used the Euro NCAP sine with dwell manoeuvre [10] that uses the yaw rate damping after a fast, transient steering input as metric. This is combined with a criterion of spin-out, which is defined as a vehicle heading angle greater than 90° at $4s$ after completion of the steer manoeuvre [11]. The results indicate that RDB increases the front steer angle threshold before vehicle spin-out is reached compared to an uncontrolled (baseline) vehicle. ARS increases this threshold on average more than RDB. They also concluded that RDB retains vehicle responsiveness better than ARS, but RDB worsens lateral stability at extreme oversteer scenarios when wheel lock-up occurs. This is due to the rear tyres saturating during braking, drastically reducing the tyres' ability to develop and maintain lateral forces.

Several studies have integrated ARS and differential braking according to the stability index (SI) [12,13]. The latter's authors note that ARS provides some advantages over differential braking, specifically that drivers do not prefer frequent differential braking intervention and that braking leads to a decrease in vehicle speed, potentially affecting fuel consumption or battery life. Differential braking should

consequently be reserved for more severe LOC scenarios and care should be taken not to have wheel lock-up occur. The proposed solution of both studies is to have the rear steering operate when the vehicle is within the stable phase plane region and combine ARS and RDB once outside the stable region.

Other methods of integration include the optimum control strategy [14] which distributes longitudinal and lateral tyre forces according to an optimum cost function. The function is a sum of the percentage friction used for all four tyres which includes a weighting coefficient per tyre. Joa & Sohn [15] employ differential braking once the rear tyres have reached the non-linear lateral response region. Of the two methods, the first relies on accurately estimating tyre force, which is technically challenging, especially during off-road driving, and the second relies on knowing the rear axle slip angle which can be estimated by use of the vehicle yaw rate, CG location and vehicle velocity, or directly measured [16].

The studies referred to in this section consider only on-road performance while similar studies for off-road conditions are scarce and those that are accessible [17,18] focus on vertical or longitudinal vehicle motion. This highlights the need for off-road ICC performance studies, especially for handling and lateral stability. This study aims to address the gap between on-road and off-road ICC for vehicle lateral stability by exploring the use of select integrated systems on rough terrain.

Vehicle simulation model

A Land Rover Defender is used as the development platform in this study. The Land Rover Defender is a typical example of a SUV with a high centre of gravity and a soft suspension. A 17-DOF non-linear Adams [19] model was previously developed and validated experimentally for lateral and vertical dynamics by [20], with improvements

to the suspension model by [21] and experimental validation of the longitudinal dynamics by [22,23]. A steering controller developed and implemented by [24] was available for this investigation. An experimentally validated FTire [25] tyre model developed by [26] was used throughout. Figure 1 shows the model topology and the model parameters are listed in Table 1. For the purposes of this study, actuator models were included for both the braking system (developed by [23]), and the rear wheel steering (added by the authors).

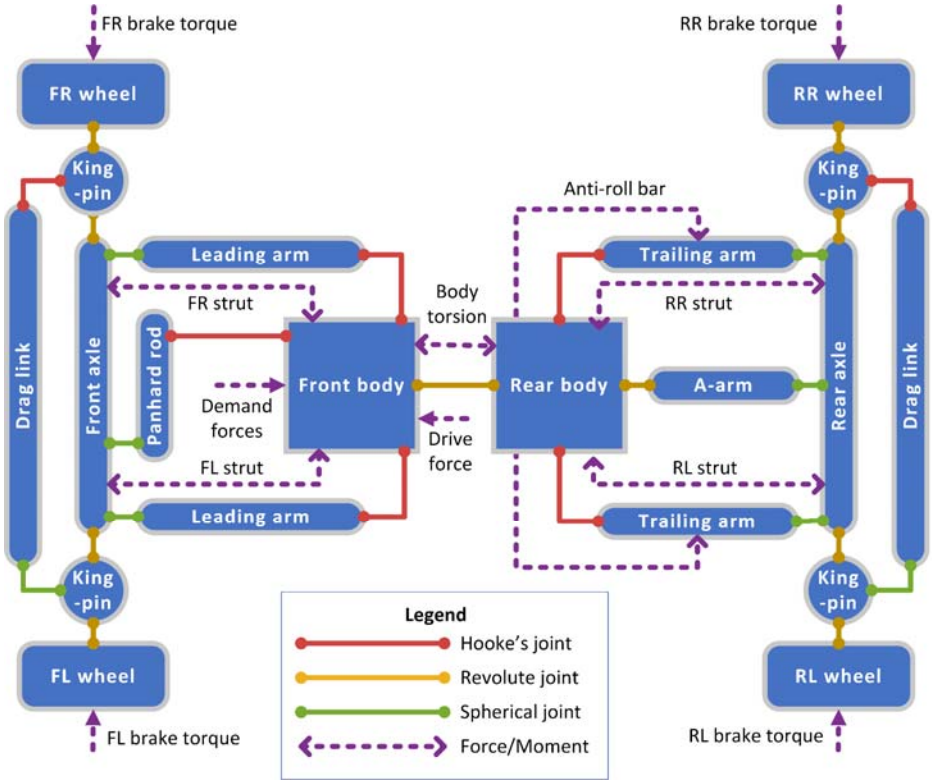

Figure 1. Graphical model topology of vehicle simulation model

Table 1. Vehicle simulation model parameters [27]

Property	Symbol	Value	Unit
Total vehicle mass	m	2047	kg
Vehicle sprung mass	m_s	1582	kg
Mass moment of inertia around vertical axis	I_{zz}	2057	kgm^2
Longitudinal distance from CG to front axle	l_f	1.55	m
Longitudinal distance from CG to rear axle	l_r	1.25	m
Track width (front and rear)	t_w	1.49	m
Effective rolling radius	r_e	0.386	m
Vehicle width	t_v	1.86	m

While the vehicle dynamics and constraints are all modelled in Adams, all control aspects are executed using MATLAB/Simulink [28] in co-simulation with the Adams model. The simulation model attains the desired speed by applying a force in the forward direction at the vehicle CG. Brake torques are applied to each wheel, and a front and rear steering angle is applied to the front right and rear right kingpins, respectively. The brake torque and steering inputs are determined in MATLAB/Simulink and fed to the Adams model. The model response is then provided as feedback from the Adams model to MATLAB/Simulink.

Simulations are performed on both a smooth road and a rough road. The rough road is an ISO8608:2016 [29] Class D road. Reference to a smooth road refers to a level road with a flat profile. A high surface friction coefficient is used for the tyre-road interface ($\mu = 1.0$) and all driving manoeuvres for this study are done at an initial speed of 60 km/h.

Control system design

3.1 Stability control reference models

Two reference models are considered for the ARS and RDB sliding mode controllers (SMCs), namely the phase plane location error (PPLE) and kinematic model reference error (KMRE).

3.1.1 Phase plane location error (PPLE)

Phase planes visualize the relationship between two state variables such as yaw rate against sideslip angle or sideslip rate against sideslip angle where the ideal relationship should be linear around the origin. This represents a stable vehicle with predictable response for the average driver. Of the two phase plane types mentioned, sideslip angle against sideslip rate ($\beta - \dot{\beta}$) is a better indication of vehicle stability [13]. Phase planes use instantaneous vehicle states such as front steering angle, rear steering angle, vehicle speed and surface friction to generate locus curves of vehicle states at that instant. A change in one or all of those variables affect the phase-portrait.

Based on a sideslip angle against sideslip rate phase plane, Chen et. al. [30] defines the SI as in Equation 1, where values of $SI = 1$ form an ellipse that encloses a portion of the linear $\beta - \dot{\beta}$ region. Values of $SI \leq 1$ represent a vehicle state inside, and values of $SI > 1$ represent a vehicle state outside the $SI = 1$ ellipse.

$$Stability\ index\ (SI) = \frac{\beta^2}{c_1^2} + \frac{\dot{\beta}^2}{c_2^2} \tag{1}$$

The vehicle phase-portrait is generated by solving Equation 2 and 3 with a zero front/rear steering angle where tyre lateral force is obtained using the non-linear Pacejka 89 (89 MF) tyre model [31]. Figure 2 shows the resulting phase portrait and indicates

the determined $SI = 1$ boundary for parameter values $c_1 = 1$ and $c_2 = 2$, defined conservatively to allow for stability control intervention in the linear $\beta - \dot{\beta}$ region and to ensure activation during manoeuvres for this study.

$$\dot{\beta} = \frac{F_{yf} + F_{yr}}{mv_x} \times 57.296 - \dot{\psi} \tag{2}$$

$$\ddot{\psi} = \left(\frac{l_f F_{yf} - l_r F_{yr}}{I_{zz}}\right) \times 57.296^2 \tag{3}$$

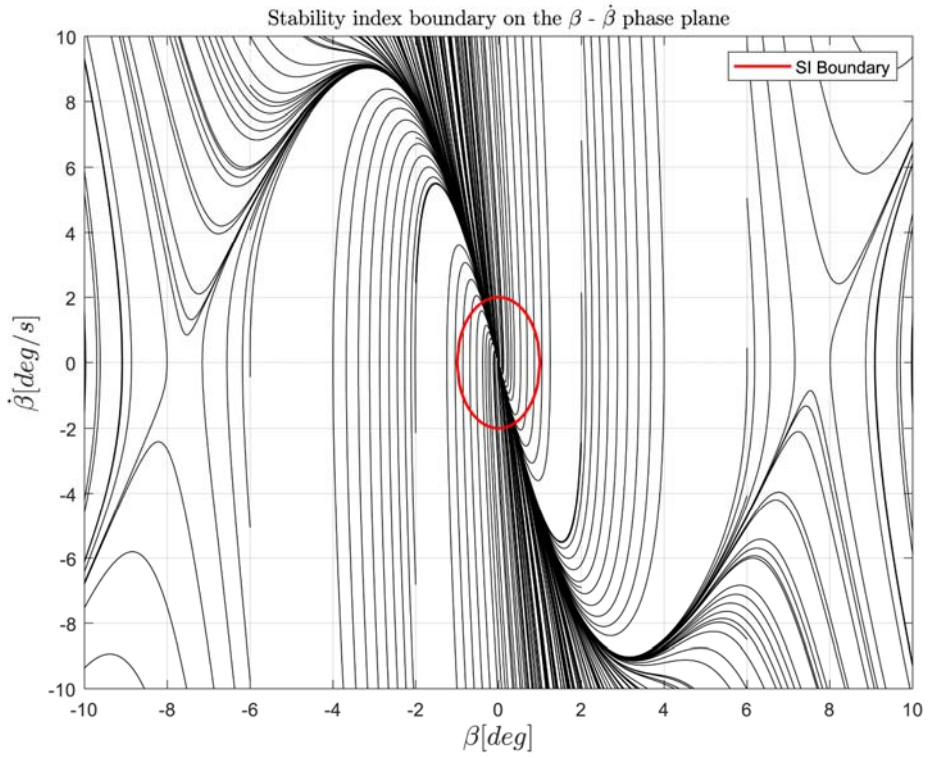

Figure 2. Experimental platform vehicle $\beta - \dot{\beta}$ phase portrait for zero front/rear steer angle at 60 km/h

A sliding mode controller (SMC) sliding variable which reduces vehicle presence in the $SI > 1$ region is proposed in Equation 4 with conditions given in Equations 5 and 6.

$$s = \left(\dot{\beta} - \dot{\beta}_{ref} + \zeta\left(\beta - \beta_{ref}\right)\right) \times \frac{1}{57.296} \tag{4}$$

$$\beta_{ref} = \begin{cases} \beta_{boundary} \times sgn(\beta) & |\beta| \geq \beta_{boundary} \\ \beta & |\beta| < \beta_{boundary} \end{cases} \tag{5}$$

$$\dot{\beta}_{ref} = \begin{cases} \dot{\beta}_{boundary} \times sgn(\dot{\beta}) & |\dot{\beta}| \geq \dot{\beta}_{boundary} \\ \dot{\beta} & |\dot{\beta}| < \dot{\beta}_{boundary} \end{cases} \tag{6}$$

Where $\beta_{boundary}$ and $\dot{\beta}_{boundary}$ are determined by the straight line connecting the sampling point outside the stability region with the phase plane origin and noting the intersection with the boundary. This process is represented by Equation 7 to Equation 9.

$$\beta_{boundary} = \sqrt{\frac{1}{\frac{m_{grad}^2}{c_2^2} + \frac{1}{c_1^2}}} \tag{7}$$

$$\dot{\beta}_{boundary} = m_{grad} \times \beta_{boundary} \tag{8}$$

$$m_{grad} = \frac{\dot{\beta}}{\beta} \tag{9}$$

3.1.2 Kinematic model reference error (KMRE)

The KMRE contrasts actual vehicle lateral state with a 2-DOF yaw plane kinematic model of the experimental platform vehicle. Gillespie [32] defines the yaw rate of a single-track kinematic vehicle model as in Equation 10.

$$\dot{\boldsymbol{\psi}}_{\boldsymbol{des}} = \frac{\mathbf{1}}{\frac{\boldsymbol{L}}{\boldsymbol{v_x}} + \frac{\left(\frac{\boldsymbol{w_f}}{\boldsymbol{C_f}} - \frac{\boldsymbol{w_r}}{\boldsymbol{C_r}}\right)}{\mathbf{57.296}\boldsymbol{g}}\ \boldsymbol{v_x}}\ \boldsymbol{\delta_f} = \frac{\mathbf{1}}{\frac{\boldsymbol{L}}{\boldsymbol{v_x}} + \frac{\boldsymbol{K_{US}}}{\mathbf{57.296}\boldsymbol{g}}\ \boldsymbol{v_x}}\ \boldsymbol{\delta_f} \tag{10}$$

Assuming small sideslip angle and rate, Rajamani [33] proposes a maximum yaw rate as in Equation 11, which allocates 85% of the available surface friction limit to the yaw rate and the remaining 15% to the sideslip component.

$$\dot{\psi}_{\lim} = \left(0.85\frac{\mu g}{v_x}\right) \times 57.296 \tag{11}$$

The reference yaw rate becomes as formulated in Equation 12.

$$\dot{\psi}_{ref} = \begin{cases} \dot{\psi}_{des} & |\dot{\psi}_{des}| \leq \dot{\psi}_{\lim} \\ \dot{\psi}_{\lim} \times sgn(\dot{\psi}_{des}) & |\dot{\psi}_{des}| > \dot{\psi}_{\lim} \end{cases} \tag{12}$$

Similarly, a reference sideslip angle based on the kinematic model is formulated in Equation 13 to Equation 14 [32].

$$\boldsymbol{\beta_{des}} = \frac{\boldsymbol{57.3c}}{\boldsymbol{R}} - \boldsymbol{\alpha_r} = \frac{\boldsymbol{57.3c}}{\boldsymbol{R}} - \frac{\boldsymbol{w_f v_x^2}}{\boldsymbol{C_f g R}} \tag{13}$$

$$R = \left(57.3 \times L + \left(\frac{w_f}{C_f} - \frac{w_r}{C_r}\right)\right)\frac{1}{\delta_f} = (57.3 \times L + K_{US})\frac{1}{\delta_f} \tag{14}$$

The desired sideslip angle is limited by the average slip angle of the rear wheels at which non-linearity starts, assumed to be 3°. The sideslip angle limit can be formulated in Equation 15 with R defined in Equation 14.

$$\beta_{\lim} = \frac{57.3c}{R} - (3 - \delta_r) \tag{15}$$

The reference sideslip then angle becomes:

$$\beta_{ref} = \begin{cases} \beta_{des} & |\beta_{des}| \leq \beta_{\lim} \\ \beta_{\lim} \times sgn(\beta_{des}) & |\beta_{des}| > \beta_{\lim} \end{cases} \tag{16}$$

An SMC sliding variable which would reduce the difference between actual and kinematic model yaw rate and sideslip is formulated in Equation 17. The understeer gradient for the kinematic model is taken as $K_{US} = 0.5$ whereas the vehicle has an understeer gradient of $K_{US} = -0.4$. The value $K_{US} = 0.5$ ensures that the reference model exhibits understeer and represents the actual vehicle CG moved forward by 5% of the wheelbase.

$$s = \left(\dot{\psi} - \dot{\psi}_{ref} + \zeta\left(\beta - \beta_{ref}\right)\right) \times \frac{1}{57.296} \tag{17}$$

3.2 Integrated chassis control system

3.2.1 Decision layer construction

The decision layer contains the two SMCs, one for ARS and one for RDB, that determine the corrective yaw moment to be generated by the steering and braking systems, respectively. The layer requires a reference model, along with an integration rule for integrating the ARS and RDB stability controllers (SCs). This study considers the rear axle slip angle and stability index (SI) as integration rules.

By combining the two reference models and the two integration rules, several different decision layer configurations are possible. Table 2 indicates the configurations investigated in this study.

Table 2. The different decision layer configurations investigated in this study

Configuration	Stability control reference model	ARS-RDB Integration rule
1	Phase plane location error (PPLE)	a. ARS on by default b. When $\alpha_r \geq 3°$, RDB is activated c. When $\alpha_r < 3°$, RDB is deactivated
2	Kinematic model reference error (KMRE)	a. ARS on by default b. When $\alpha_r \geq 3°$, RDB is activated c. When $\alpha_r < 3°$, RDB is deactivated
3	Kinematic model reference error (KMRE)	a. ARS on by default b. When $SI \geq 1$, RDB is activated c. When $SI < 1$, RDB is deactivated

Figure 3 shows the decision layer block diagram, where block 1 encloses the three configurations as listed in Table 2, and block 2 the moment to force conversion which is according to Equation 18 and Equation 19.

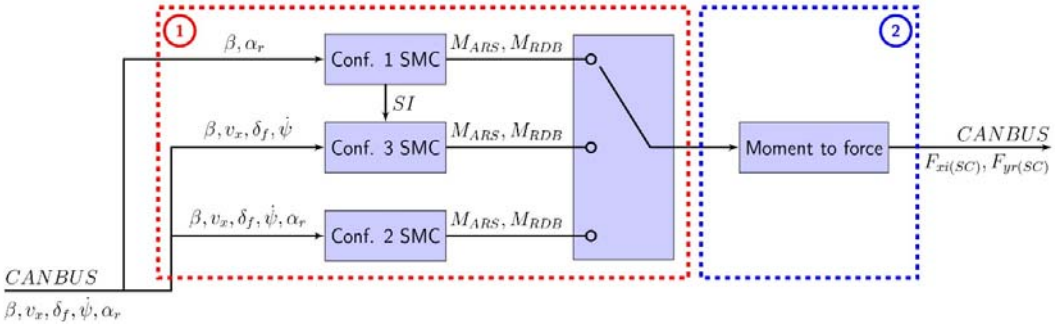

Figure 3. The decision layer block diagram

$$\boldsymbol{F_{yr(SC)} = \frac{M_{ARS}}{l_r}} \tag{18}$$

$$\boldsymbol{F_{x3(SC)} = \begin{cases} \frac{M_{RDB}}{\frac{tw}{2}} & M_{RDB} > 0 \\ 0 & M_{RDB} \leq 0 \end{cases}} \tag{19}$$

$$F_{x4(SC)} = \begin{cases} \frac{M_{RDB}}{\frac{tw}{2}} & M_{RDB} < 0 \\ 0 & M_{RDB} \geq 0 \end{cases}$$

3.2.2 Control layer construction.

The control layer receives setpoints of braking force for each rear wheel and the additional lateral force required of the rear wheels from the decision layer. The layer performs two functions for the RDB and two for the ARS systems. For the RDB system (Figure 4), block 1 encloses the functions that determine the required slip ratio and angular velocity for each wheel while the functions in block 2 determine the reference brake line pressure based on the wheel speed error through a PID controller. For the ARS system (Figure 5), the function in block 1 determines the current average rear axle slip angle, which acts as the centre point about which the additional lateral force is based, while the function in block 2 determines the rear steering angle to generate the required additional rear lateral force.

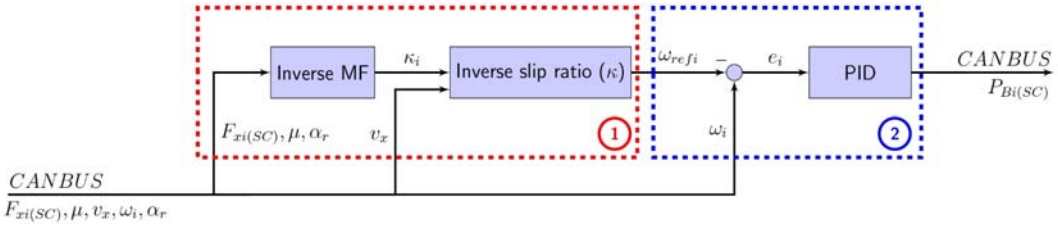

Figure 4. The rear differential braking (RDB) control layer block diagram

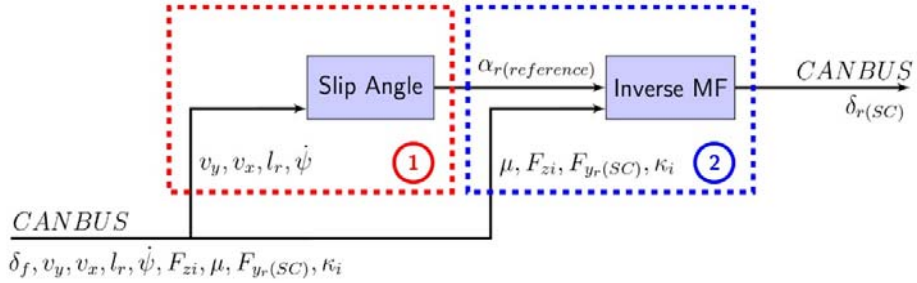

Figure 5. The active rear steering (ARS) control layer block diagram

RDB physical layer construction.

The test vehicle (on which the simulation model is based) is equipped with an ABS modulator where differential braking is achieved by a linear actuator that preloads the ABS modulator's accumulator before a differential braking manoeuvre. The differential braking system can be modelled as a first order delay with a time constant of $\tau = 0.2\ s$ [23]. The physical brake emulating block diagram is shown in Figure 6, where the block functions from left to right are: the ABS modulator with first order delay, a saturation function to limit brake hydraulic pressure to 10 MPa and a gain that converts brake calliper pressure to disc applied torque. The gain has a value of $K_\tau = 271$ [23].

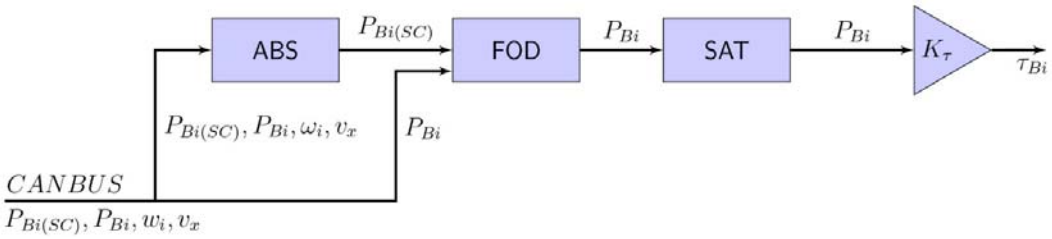

Figure 6. The physical brake emulating block diagram

ARS physical layer construction.

Figure 7 shows the ARS emulating block diagram, where the functions from left to right are: a PID controller to converge setpoint and actual rear steering angle, a $\pm 12V$ saturation block, the linear actuator model, a $\pm 11\ mm$ displacement saturation block and a gain $K_1 = 3.67 \times 10^{-3}$ to convert actuator displacement from mm to rear steering angle. The characteristics of the ARS hardware are based on the rear wheel steering geometry, assuming small angles.

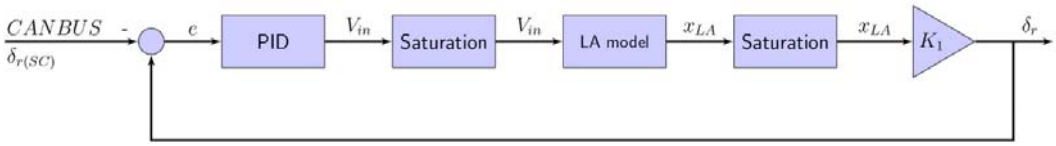

Figure 7. The active rear steering emulating block diagram

Decision layer SMC gain selection

Since the integrated controller makes use of a supervisory control structure, both ARS and RDB should be able to operate as stand-alone SCs, which require tuning the SMC gain and SMC zeta weighting of both SMCs individually. This study considers zeta weighting values of 0, 0.5, 1 or 2 , which represent: no consideration for sideslip error, half weighting, same weighting and double weighting of the sideslip error. Combining the variety of ARS or RDB with different zeta weightings and two possible SC reference models operating on two possible road classifications, results in 32 system combinations as listed in Table 3.

Table 3. Different system combinations based on control strategy, SC reference model, road classification and zeta weighting

System combination	Control strategy	Stability control reference model	Road classification	Group	Zeta weighting	Gain
1	ARS	Phase plane location error SMC sliding variable: $s = \dot{\beta} - \dot{\beta}_{ref} + \zeta(\beta - \beta_{ref})$	Smooth	A	0	5000
2					0.5	3000
3					1	3000
4					2	3000
5			Rough	B	0	8000
6					0.5	9000
7					1	9000
8					2	8000
9		Kinematic model reference error SMC sliding variable: $s = \dot{\psi} - \dot{\psi}_{ref} + \zeta(\beta - \beta_{ref})$	Smooth	C	0	2500
10					0.5	3500
11					1	4000
12					2	4000
13			Rough	D	0	2000
14					0.5	2000
15					1	2000
16					2	2000
17	RDB	Phase plane location error SMC sliding variable: $s = \dot{\beta} - \dot{\beta}_{ref} + \zeta(\beta - \beta_{ref})$	Smooth	E	0	1500
18					0.5	1500
19					1	50
20					2	1000
21			Rough	F	0	7000
22					0.5	6000
23					1	1000
24					2	6000
25		Kinematic model reference error SMC sliding variable: $s = \dot{\psi} - \dot{\psi}_{ref} + \zeta(\beta - \beta_{ref})$	Smooth	G	0	3
26					0.5	2.5
27					1	2
28					2	2.5
29			Rough	H	0	3
30					0.5	3
31					1	3.5
32					2	3

The SMC gain per system is empirically obtained by cycling through a series of SMC gains and determining which gain value minimises the sum of the squared sliding variable over the duration of a manoeuvre (Figure 8). The gain which minimizes Equation 20 is the chosen system combination SMC gain. This method identifies the SMC gain which causes the respective SMC to best approximate the appropriate reference model and does not account for vehicle lateral displacement error on a set path.

$$q = \sum_{i=1}^{n}(s^2) \tag{20}$$

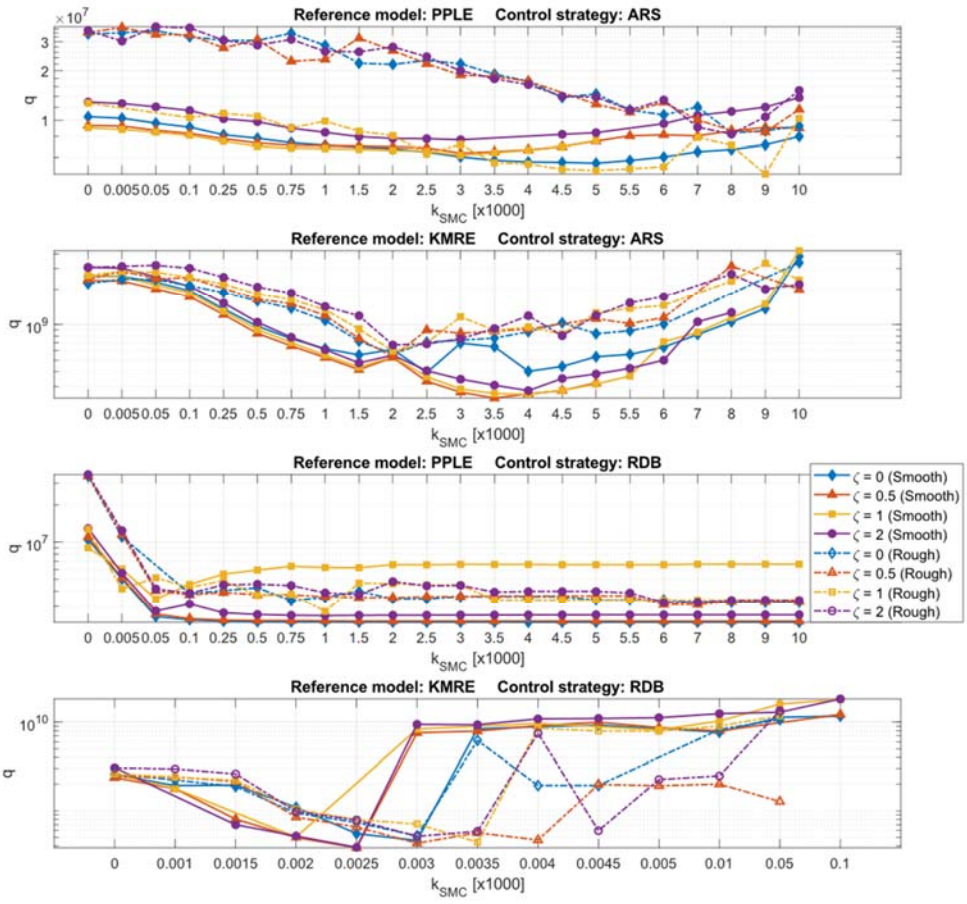

Figure 8. Sum of squared sliding variable for increasing SMC gain of Table 3 system combinations

The manoeuvre performed for the SMC gain tuning process is the sine with dwell front steering input with a steering amplitude of 3.5°, as it is an open-loop manoeuvre with high repeatability that facilitates a direct comparison of different SMC gain values. An amplitude of 3.5° is chosen because it is the observed steering amplitude when the driver model performs a closed-loop DLC at 60 km/h. The manoeuvre is performed for a right-side lateral offset, since the test vehicle is right-hand drive. Figure 8 shows that

the optimal SMC gain for the same system with different zeta weightings is in a similar value range, while the same system for different terrains have different optimal SMC gain values. This indicates that the optimal SMC gain is sensitive to terrain.

Decision layer SMC zeta weighting selection.

One appropriate zeta weighting per Group A-H of Table 3 is selected based on four performance metrics:

(1)Yaw rate ratio (YRR_{1s}) taken at 1s from completion of steer (COS).

(2)Yaw rate ratio ($YRR_{1.75s}$) taken at 1.75s from completion of steer (COS).

(3)Maximum lateral displacement (ΔY_{CG}) at 1.07s from beginning of steer (BOS).

(4)Maximum roll angle during manoeuvre (ϕ_{max}).

Metrics 1-3 are used by the Euro NCAP [10] to assess stability control performance during a sine with dwell steer manoeuvre. The vehicle roll angle (metric 4) is of interest for the test vehicle due to its high CG and resulting rollover propensity [27].

Normalized metric values are represented by radar plots shown in Figure 9.

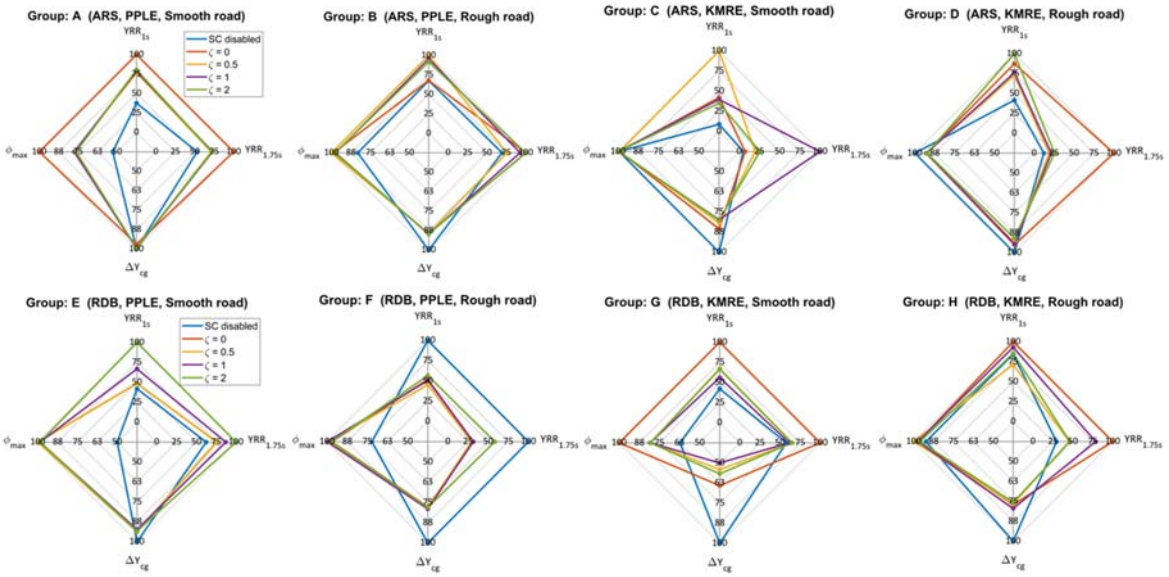

Figure 9. Radar plots for Group A-H of Table 3

Table 4. The Table 3 system combination numbers which comprise the stand-alone and integrated systems

System type	System name for this study	Stability control reference model	Default: Table 3 system no. on road classification		Switches to: Table 3 system no. on road classification		Integration parameter
			Smooth	Rough	Smooth	Rough	
Stand-alone sub-system SC	ARS, PPLE	Phase plane location error	1	8	-	-	-
	ARS, KMRE	Kinematic model reference error	11	13	-	-	-
	RDB, PPLE	Phase plane location error	20	24	-	-	-
	RDB, KMRE	Kinematic model reference error	25	29	-	-	-
Integrated sub-system SC	ICC Conf. 1	Phase plane location error	1	8	20	24	α_r
	ICC Conf. 2	Kinematic model reference error	11	13	25	29	α_r
	ICC Conf. 3	Kinematic model reference error	11	13	25	29	SI

The largest polygon per Group A-H, as quantified by Equation 21, represents the best

overall performing zeta weighting for that group. Based on this criteria, Table 4 defines the unique system numbers that make up the ARS, RDB and integrated systems for this study.

$$Polygon\ area = \frac{1}{2} \times (YYR_{1s} \times (YYR_{1.75s} + \phi_{max}) + \Delta Y_{CG} \times (YYR_{1.75s} + \phi_{max})) \quad (21)$$

Simulation results

The model of the test vehicle with the different control system configurations is subjected to closed-loop testing where the vehicle is driven through a DLC manoeuvre [34] with a driver model [35] on a smooth and rough road. Performance indicators are the path following ability, peak absolute roll angle, -yaw rate and -sideslip angle and DLC section 5 exit speed. Path following ability is assessed by checking whether the vehicle is able to keep within cones placed on either side of the path [34]. This study represents the CG point location on either side of the reference path which would likely result in the vehicle knocking over the cones.

Figure 10 shows the performance of the SCs using the PPLE reference model, along with the SC disabled (baseline) vehicle. The displacement plot shows that the controllers tend to overshoot in DLC sections 5 and 6, with only the RDB controller maintaining the vehicle within the CG boundary. All controllers improve the peak absolute yaw rate and -sideslip angle with a lower value, while worsening peak absolute roll angle with a higher value. Of these controllers, RDB has the lowest exit speed, followed by ICC Conf. 1, reinforcing that brake-based systems have the lowest exit speed. The results indicate that PPLE SCs do not tend to improve path following although improving peak absolute yaw rate and -sideslip angle.

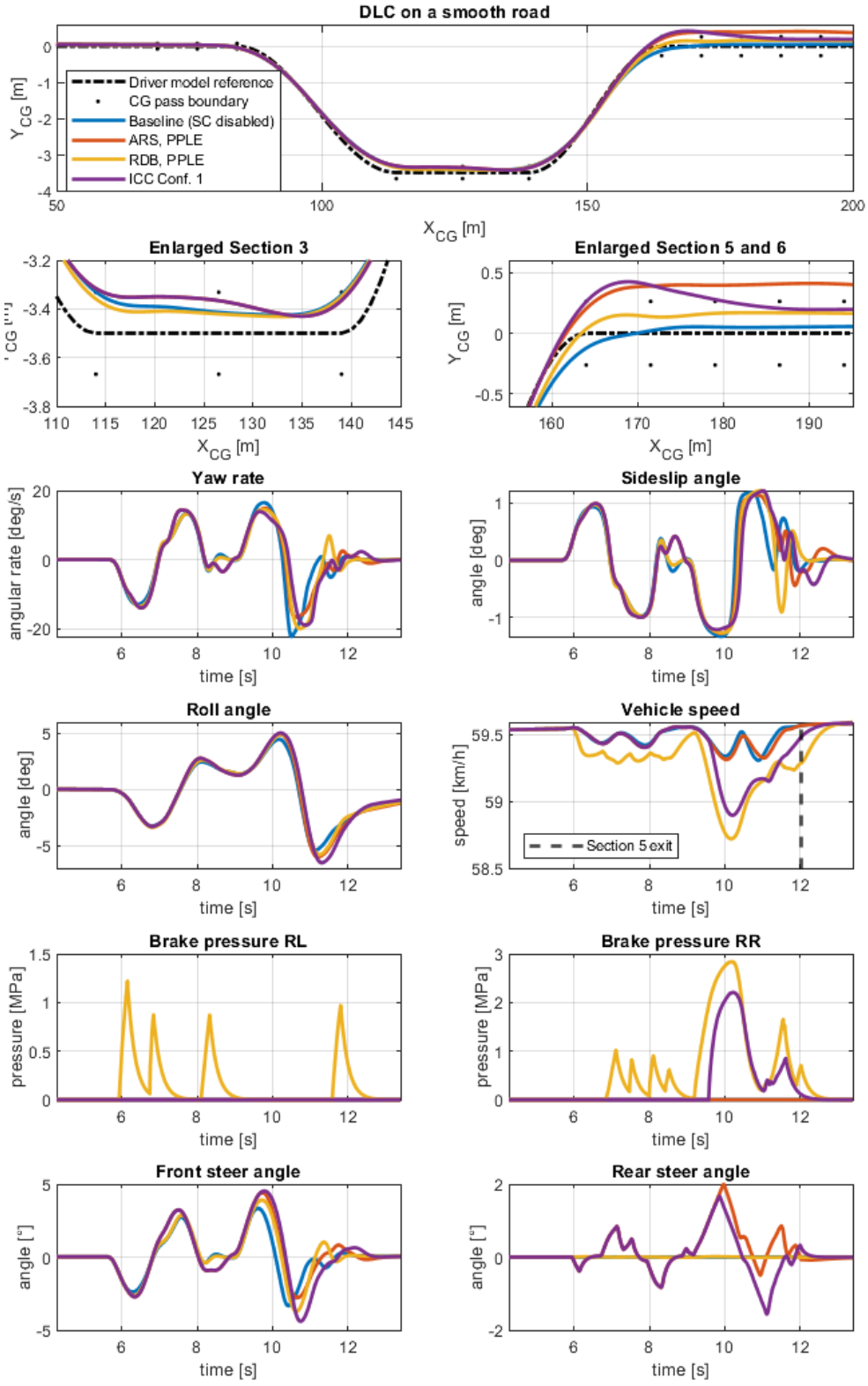

Figure 10. Smooth road PPLE reference model SC system performance

Figure 11 shows the performance of SCs using the KMRE reference model compared to baseline. The plots show that the SCs improve path following ability in DLC section 3, but ICC Conf. 3 shows overshoot and worsened path following in section 5 and 6. RDB integration for ICC Conf. 2 only occurs around the 11s mark, which is after peak absolute yaw rate and sideslip angle events have occurred, thus the response of the ARS and ICC Conf. 2 systems are virtually the same up to that instant. The ARS (and ICC Conf. 2) SCs improve the peak absolute yaw rate, while RDB shows a result similar to the baseline. The peak absolute yaw rate of ICC Conf. 3 is the worst of all the configurations, including the baseline. A similar observation is made for sideslip angle. Peak absolute roll angle shows that the RDB and ICC Conf. 3 SCs have the highest values, while the ARS (and ICC Conf. 2) SCs show a response similar to the baseline. The ICC Conf. 3 and RDB SCs have the lowest exit speed while ARS shows a value similar to the baseline configuration and ICC Conf. 2 a slightly worse than baseline value. The results indicate that KMRE SCs tend to improve path following although having absolute yaw rate and sideslip angle values comparable to baseline peak values.

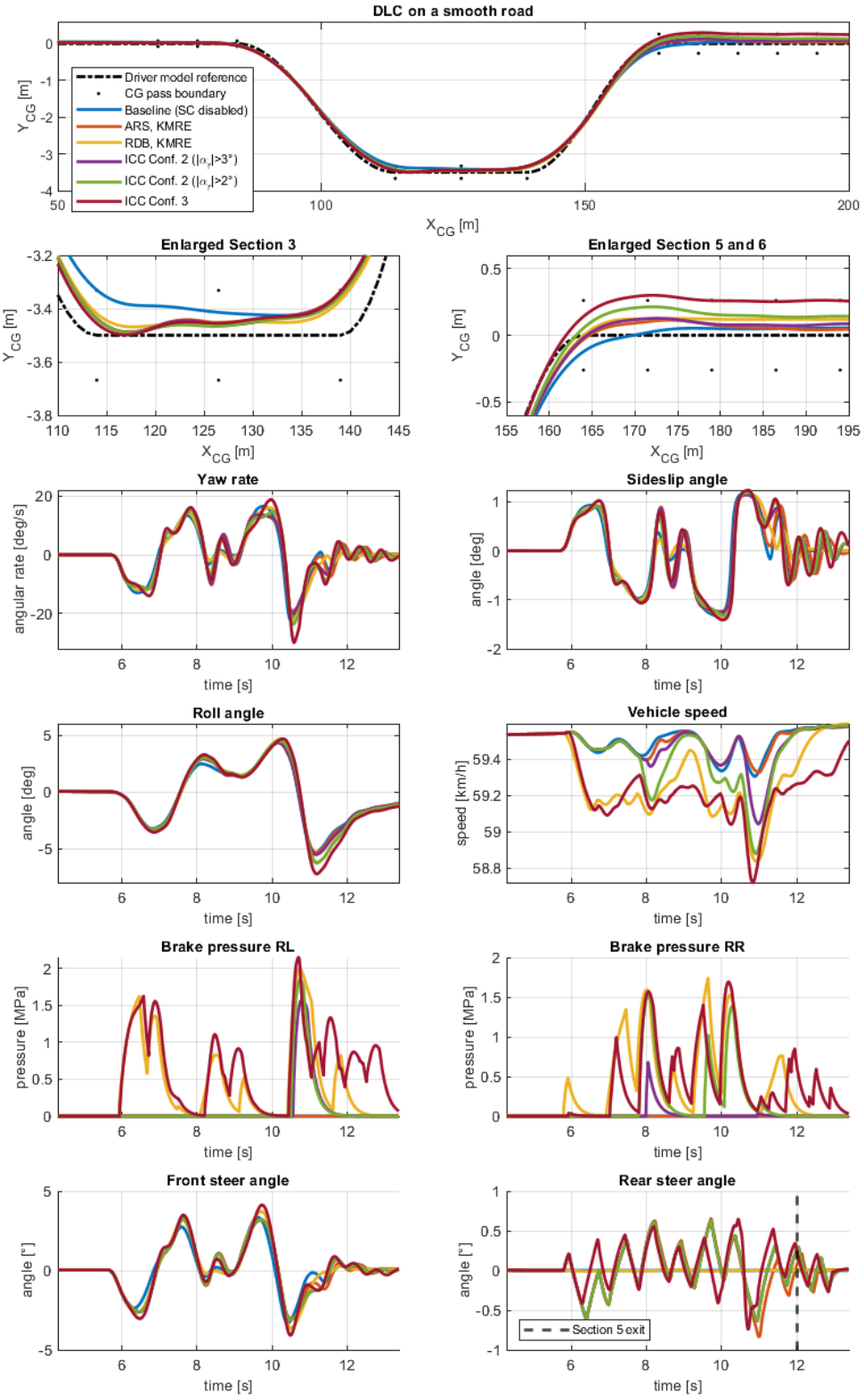

Figure 11. Smooth road KMRE reference model SC system performance

Of all the integrated controllers, ICC Conf. 2 shows potential as both the ARS and RDB (KMRE) systems pass the DLC test, and it is also the only integrated system that passes the test (no cones hit). It may be possible to lower the integration threshold so that RDB integration occurs earlier in the manoeuvre. To illustrate this, "ICC Conf. 2 ($|\alpha_r|$>2°)" simulation results were also included in Figure 11. The displacement plot shows that the adapted ICC Conf. 2 has a displacement lying somewhere between that of ARS and RDB for section 3, with a larger overshoot than either system in section 5. The peak absolute yaw rate, -sideslip angle, and roll angle also tend toward the RDB response. The exit speed of the adapted ICC Conf. 2 is comparable to the entry speed, which is similar to the ARS system and an improvement on the RDB system. It is evident that tuning of the rear axle slip angle integration rule biases ICC Conf. 2 response to be more or less similar to ARS or RDB behaviour.

Figure 12 shows the response of the rough road PPLE SCs. The plots indicate that none of the controllers were able to keep the vehicle within bounds, with ARS showing the worst performance. This performance is somewhat improved by ICC Conf. 1, which tends towards RDB behaviour. RDB is the only controller that improved peak absolute yaw rate and sideslip angle, with ARS showing the worst performance and ICC Conf. 1 a response between that of ARS and RDB. In terms of peak absolute roll angle, RDB is similar to baseline while ARS is the worst performer and ICC Conf. 1 between that of ARS and RDB. The RDB system has the lowest exit speed, which is somewhat improved by the integrated controller since ARS has the highest exit speed of all SCs. As with the smooth road PPLE SCs, the SCs tend to not improve path following.

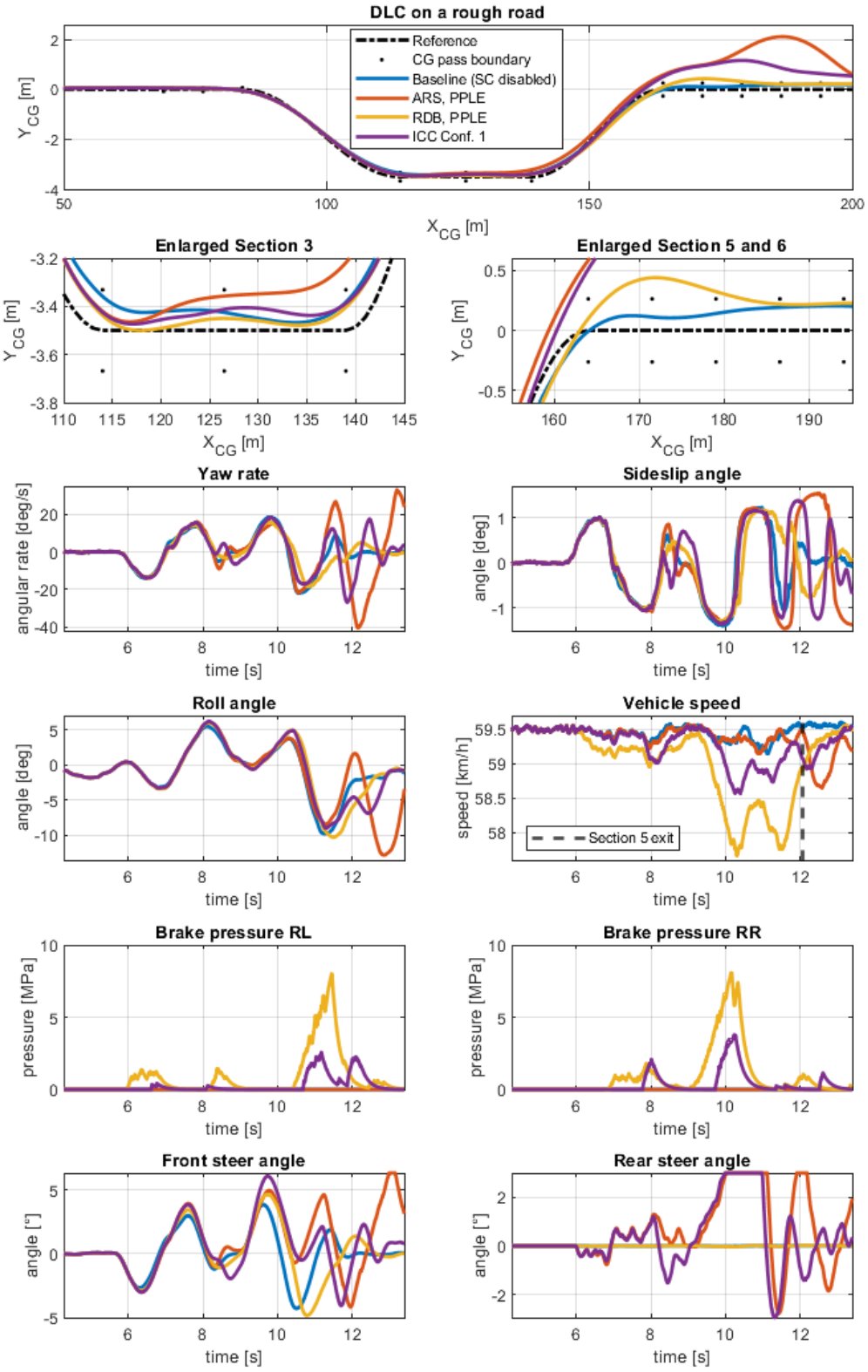

Figure 12. Rough road PPLE reference model SC system performance

Figure 13 shows the performance of the rough road SCs using the KMRE reference model, compared to baseline. Only ICC Conf. 2 with the original integration rule ($|\alpha_r| > 3°$) is considered in this paragraph, with alternative integration rule ($|\alpha_r| > 2°$) results discussed in the following paragraph. The displacement plots show that all SCs improve path following ability in section 3, with varying results in section 5 and 6, although remaining within bounds. The RDB system shows the nearest to reference displacement in section 5 and ARS the worst, with the displacement performance of both ICC Conf. 2 and Conf. 3 between that of ARS and RDB. When considering the peak absolute yaw rate, ARS has the worst value, while all other systems improve on the baseline. The peak absolute sideslip angle performance of all systems is similar to baseline while ICC Conf. 3 and RDB have a similar to baseline peak absolute roll angle with ARS and ICC Conf. 2 showing an improvement. In terms of exit speed, RDB and ICC Conf. 3 have the lowest values while ICC Conf. 2 and ARS are similar to baseline. As with the KMRE SCs on a smooth road, the SCs tend to improve path following while having comparable to baseline peak absolute yaw rate and sideslip angle.

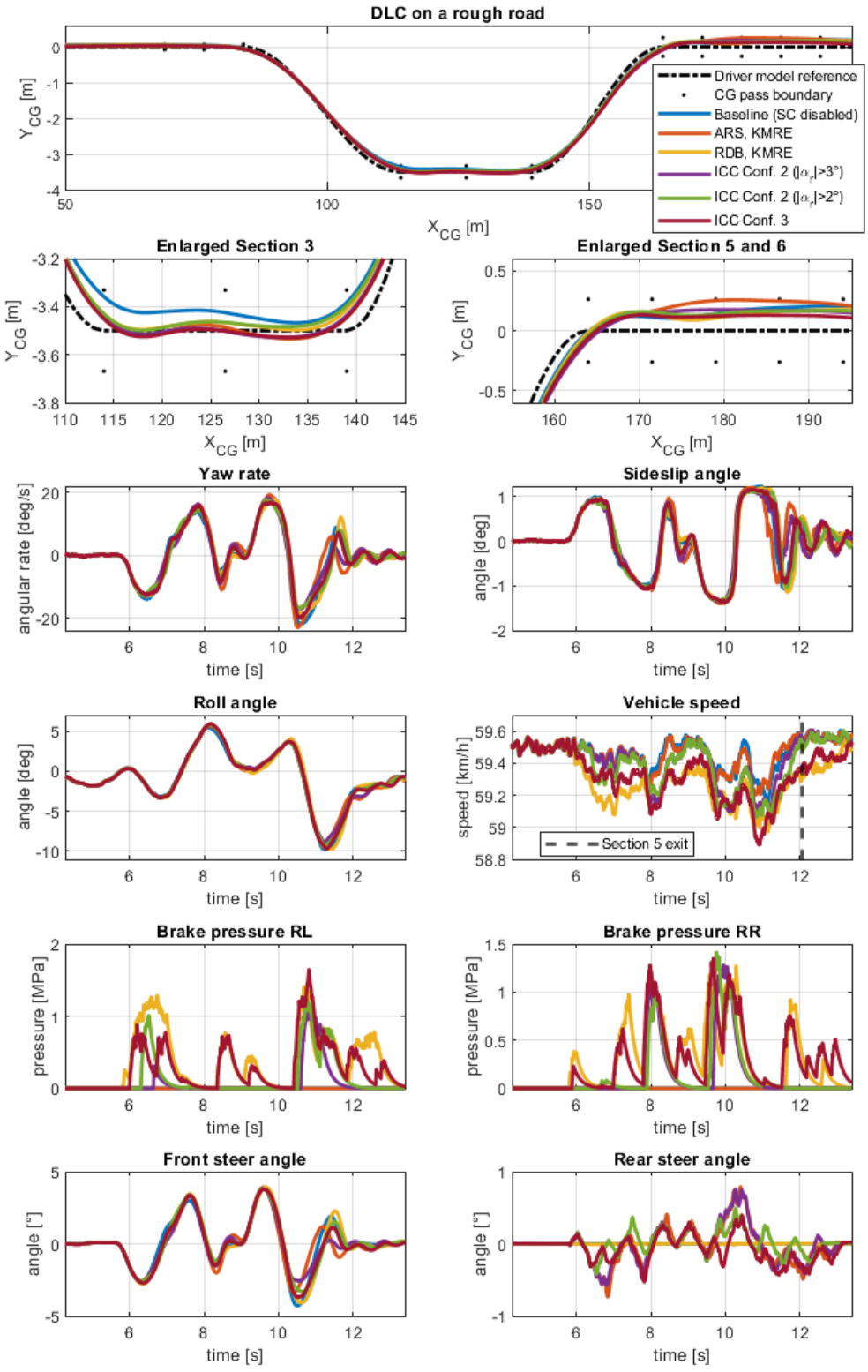

Figure 13. Rough road KMRE reference model SC system performance

Analysis of ICC Conf. 2 is further explored by lowering the integration threshold so that RDB is integrated when $|\alpha_r| > 2°$. The results are shown in Figure 13 and indicate that the effect on the displacement is to approximate RDB response more than for when RDB is integrated when $|\alpha_r| > 3°$. The same observation is made for roll angle, whereas peak absolute yaw rate, sideslip angle and vehicle speed remain largely the same. As with KMRE SCs on a smooth road, it is observed that tuning of the integration threshold biases system response towards either ARS or RDB behaviour.

Conclusions and future work

The study aimed to investigate whether the integration of active rear steering (ARS) and rear differential braking (RDB) may improve off-road vehicle lateral stability and how the performance of such systems compare on smooth and rough roads. The effect of key design choices such as stability control reference model, SMC gain and integration rule were also considered.

It was found that SCs with the kinematic model reference error (KMRE) tended to improve lateral stability, as measured by reference path offset, while those with the phase plane location error (PPLE) tended to not show the same improvement, although improving peak absolute yaw rate and -sideslip angle if the vehicle did not lose control. These properties of the PPLE reference model are desirable but negatively affect the path following ability of the vehicle and may leave the vehicle feeling unresponsive to the driver. The KMRE SC reference model is useful for allowing large yaw rate and sideslip angle peak development while being good at damping those responses once the manoeuvre is complete. This was observed for both terrains.

The gain of the SMC, which determines the corrective yaw moment, appears sensitive to terrain type as the optimal gain setting was different for the two terrains. It may be useful to maintain the gain on the optimal setting for a terrain type.

Integrated systems using the rear axle slip angle as integration rule show a response between that of ARS and RDB, whereas the same observation is not consistently made for the SI integration rule. Based on this observation, the rear axle slip angle is tuneable to bias system response towards either ARS or RDB behaviour. The advantage of such an integration rule is that a single tuneable parameter determines how the different SC systems are integrated. The RDB SCs consistently show good path following, but with the lowest course exit speeds while ARS SCs showed the highest DLC exit speeds. A suitably chosen rear axle slip angle integration threshold created a controller with the good path following of RDB and high exit speed of ARS, resulting in an overall more desirable system than either stand-alone RDB or ARS systems. Future work should focus on:

(1) Experimental validation of results.
(2) Creating a SMC gain schedule for a larger range of operating conditions so that the controllers may always use their optimal settings for different speeds and terrains.
(3) Developing or including existing means of accurately estimating the ISO8608:2016 road classification while driving.
(4) Investigating the effect of road adhesion on the reference values used for this study.

Nomenclature

Table 5. Nomenclature

Symbol	Description	Unit
C_f	Front axle tyre cornering stiffness	$[\frac{N}{\circ}]$
C_r	Rear axle tyre cornering stiffness	$[\frac{N}{\circ}]$
c_1	SI sideslip angle parameter	
c_2	SI sideslip rate parameter	
c	Distance from rear axle to CG	$[m]$
e	Error	
e_i	Error applicable to each wheel ($i = 1 \dots 4$)	
F_{yf}	Front axle lateral force	$[N]$
F_{yr}	Rear axle lateral force	$[N]$
$F_{yr(SC)}$	Reference additional rear lateral force	$[N]$
$F_{x3(SC)}$	Rear left longitudinal force	$[N]$
$F_{x4(SC)}$	Rear right longitudinal force	$[N]$
$F_{xi(SC)}$	Reference rear lateral force ($i = 3{,}4$)	$[N]$
F_{zi}	Tyre normal force ($i = 1 \dots 4$)	$[N]$
g	Gravity acceleration constant ($g = 9.81\ m.s^{-2}$)	$[m.s^{-2}]$
I_{ZZ}	Mass moment of inertia about the vertical axis	$[kg.m^2]$
K_1	Power screw force to torque gain	
K_{US}	Understeer gradient	$[^\circ/g]$
K_τ	Brake pressure to torque conversion gain	
L	Wheelbase	$[m]$
l_f	Distance from front axle to CG	$[m]$
l_r	Distance from rear axle to CG	$[m]$
M_{ARS}	ARS reference yaw moment	$[N.m]$
M_{RDB}	RDB reference yaw moment	$[N.m]$
m	Vehicle mass	$[kg]$
m_{grad}	Phase plane connecting line gradient	
m_s	Vehicle sprung mass	$[kg]$
P_{Bi}	Brake line pressure ($i = 1 \dots 4$)	$[MPa]$
$P_{Bi(SC)}$	Stability control reference brake line pressure ($i = 1 \dots 4$)	$[MPa]$
q	Cost function output	
R	Radius of turn	$[m]$
r_e	Effective rolling radius	$[m]$
s	SMC sliding variable	
t_v	Vehicle width	$[m]$
t_w	Track width	$[m]$

V_{in}	Motor input voltage	$[V]$
v_x	Longitudinal velocity	$[m.s^{-1}]$
v_y	Lateral velocity	$[m.s^{-1}]$
w_f	Vehicle weight apportioned to the front axle	$[kg]$
w_r	Vehicle weight apportioned to the rear axle	$[kg]$
x_{LA}	Linear actuator displacement	$[m]$
$Y_{\Delta CG}$	Maximum lateral displacement (Sine with dwell test)	$[m]$
YRR_{1s}	Yaw rate ratio at 1s after COS (Sine with dwell test)	
$YRR_{1.75s}$	Yaw rate ratio at 1.75s after COS (Sine with dwell test)	
α_r	Slip angle at the rear wheels	[°]
$\alpha_{r(ref)}$	Reference slip angle at the rear wheels	[°]
β	Sideslip angle	[°]
$\beta_{boundary}$	Phase plane sideslip angle boundary	[°]
β_{des}	Desired sideslip angle	[°]
β_{lim}	Sideslip angle at which tyre non linearity starts	[°]
β_{ref}	Reference sideslip angle	[°]
$\dot{\beta}$	Sideslip rate	$[°.s^{-1}]$
$\dot{\beta}_{boundary}$	Phase plane sideslip rate boundary	$[°.s^{-1}]$
$\dot{\beta}_{ref}$	Reference sideslip rate	$[°.s^{-1}]$
δ_f	Front wheel steering angle	[°]
δ_r	Rear wheel steering angle	[°]
$\delta_{r(SC)}$	Stability control reference rear steering angle	[°]
ζ	Sideslip angle error weighting	
κ_i	Tyre longitudinal slip ratio ($i = 1 \dots 4$)	
μ	Coefficient of friction	
τ	Time constant	$[s]$
ϕ_{max}	Maximum vehicle CG roll angle (sine with dwell test)	[°]
$\dot{\psi}$	Yaw rate	$[°.s^{-1}]$
$\dot{\psi}_{des}$	Desired yaw rate	$[°.s^{-1}]$
$\dot{\psi}_{ref}$	Reference yaw rate	$[°.s^{-1}]$
$\dot{\psi}_{lim}$	Yaw rate limit before sliding	$[°.s^{-1}]$
$\ddot{\psi}$	Yaw acceleration	$[°.s^{-2}]$
ω_i	Wheel angular velocity ($i = 1 \dots 4$)	$[°.s^{-1}]$
$\omega_{i(ref)}$	Wheel reference angular velocity ($i = 1 \dots 4$)	$[°.s^{-1}]$

References

[1] World Health Organization. Global status report on road safety. 2018 ed. France: World Health Organization; 2018. p. 4.

[2] European Patent Office. Anton van Zanten [Website]. European Patent Office; 2016 [cited 2022 12.11.2022]; Anton van Zanten: Winner of the European

Inventor Award 2016]. Available from: https://www.epo.org/news-events/events/european-inventor/finalists/2016/vanzanten.html

[3] European Commission. Advanced driver assistance systems : 2018. European Commission; 2018. p. 12-13.

[4] Papelis YE, Watson GS, Brown TL. An empirical study of the effectiveness of electronic stability control system in reducing loss of vehicle control. Accident Analysis and Prevention. 2010;42(3):929-934.

[5] Savitski D, Ivanov V, Augsburg K, et al., editors. State-of-the-art and future developments in integrated chassis control for ground vehicles. International Society for Terrain-Vehicle Systems (ISTVS); 2015; Rome.

[6] Hamersma HA, Botha TR, Els SP. The dynamic rolling radius of a pneumatic tyre on hard terrains. International Journal of Vehicle Systems Modelling and Testing. 2014;11(3):234-251.

[7] Kyriakidis M, van de Weijer C, van Arem B, et al., editors. The deployment of Advanced Driver Assistance Systems in Europe. 22nd ITS World Congress; 2015; Boreaux.

[8] Ackermann J, Bünte T, Odenthal D, editors. Advantages of active steering for vehicle dynamics control. 32nd International Symposium on Automotive Technology and Automation; 1999; Vienna.

[9] Canale M, Fagiano L. Comparing rear wheel steering and rear active differential approaches to vehicle yaw control. Vehicle Syst Dyn. 2010;48(5):529-546.

[10] European New Car Assessment Programme. The dynamic test of car electronic stablity control (ESC) systems protocol. Euro NCAP; 2011.

[11] Forkenbrock GJ, Boyd PL. NHTSA's light vehicle handling and ESC effectiveness research program. Washington: National highway traffic safety administration (NHTSA); 2008.

[12] Bardawil C, Talj R, Francis C, et al., editors. Integrated vehicle lateral stability control with different coordination strategies between active steering and differential braking. 17th International IEEE Conference on Intelligent Transportation Systems (ITSC); 2014; China.

[13] Xie X, Jin L, Jiang Y, et al. Integrated dynamics control system with ESC and RAS for a distributed electric vehicle. IEEE Access. 2018;6:18694-18704.

[14] Mokhiamar O, Abe M. How the four wheels should share forces in an optimum cooperative chassis control. Control Engineering Practice. 2006;14:295-304.

[15] Joa E, Sohn K. Integrated chassis control for vehicle stabilty under various road friction conditions. SAE international. 2018 (0552):1-10.

[16] Botes W, Botha T, Els PS. Sideslip Angle Estimation Using a Kinematics Based Unscented Kalman Filter and Digital Image Correlation. Advances in Dynamics of Vehicles on Roads and Tracks. 2020:1635-1642.

[17] Hamersma HA. ABS braking on rough terrain [Dissertation]2017. Available from: https://repository.up.ac.za/handle/2263/61607.

[18] Kat C, Els PS. Effect of Tyre Pressure on Ride Comfort from an Integrated Chassis Control Perspective. Advances in Dynamics of Vehicles on Roads and Tracks. 2019 (2019):1723-1729.

[19] MSC Software. Adams. 2019. MSC Software; 2021.

[20] Thoresson MJ, Uys PE, Els PS, et al. Efficient optimisation of a vehicle suspension system, using a gradient-based approximation method, Part 1: Mathematical modelling. Math Comput Model. 2009 Nov;50(9-10):1421-1436.

[21] Van der Westhuizen SF, Els PS. Comparison of different gas models to calculate the spring force of a hydropneumatic suspension. J Terramechanics. 2015 Feb;57:41-59.

[22] Hamersma HA. Longitudinal vehicle dynamics control for improved vehicle safety: University of Pretoria; 2013.

[23] Penny WCW, Els PS. The test and simulation of ABS on rough, non-deformable terrains. J Terramechanics. 2016 10//;67:1-10.

[24] Thoresson MJ, Botha TR, Els PS. The relationship between vehicle yaw acceleration response and steering velocity for steering control. Int J Vehicle Des. 2014;64(2-4):195-213.

[25] cosin scientific software. FTire - Flexible Structure Tire Model Modelization and Parameter Specification 2022 [11 May 2022]. Available from: https://www.cosin.eu/support/documentation/

[26] Bosch H-RB, Hamersma HA, Els PS. Parameterisation, validation and implementation of an all-terrain SUV FTire tyre model. J Terramechanics. 2016;67:11-23.

[27] Peenze AJ. Model predictive suspension control on off-road vehicles2020 [cited. https://repository.up.ac.za/handle/2263/79302

[28] MathWorks. MATLAB and Simulink 2016 [20 July 2016]. Available from: http://www.mathworks.com/

[29] International Organization for Standardization (ISO). ISO 8608:2016 - Mechanical vibration - Road surface profiles — Reporting of measured data.

[30] Chen W, Xiao H, Wang Q, et al. Integrated vehicle dynamics and control. 1 ed. Capitol Singapore: John Wiley & Sons; 2016. p. 206.

[31] Bakker E, Pacejka HB, Lidner L. A new tire model with an application in vehicle dynamics studies. SAE paper. 1989;890087:101-113.

[32] Gillespie TD. Fundamentals of vehicle dynamics. Society of Automotive Engineers (SAE); 1992.

[33] Rajamani R. Vehicle dynamics and control. Springer; 2006.

[34] International Organization for Standardization (ISO). ISO 3888-1:2018 Passenger cars - Test track for a severe lane-change manoeuvre - Part 1: Double lane-change.

[35] Botha TR. High speed autonomous off-road vehicle steering [Thesis]: University of Pretoria; 2011. Available from: https://repository.up.ac.za/handle/2263/29665.